



Disparate Individual Fates Compose Robust CD8+ T Cell Immunity

Veit R. Buchholz *et al.* Science **340**, 630 (2013); DOI: 10.1126/science.1235454

This copy is for your personal, non-commercial use only.

If you wish to distribute this article to others, you can order high-quality copies for your colleagues, clients, or customers by clicking here.

Permission to republish or repurpose articles or portions of articles can be obtained by following the guidelines here.

The following resources related to this article are available online at www.sciencemag.org (this information is current as of May 31, 2013):

Updated information and services, including high-resolution figures, can be found in the online version of this article at:

http://www.sciencemag.org/content/340/6132/630.full.html

Supporting Online Material can be found at:

http://www.sciencemag.org/content/suppl/2013/03/13/science.1235454.DC1.html

A list of selected additional articles on the Science Web sites **related to this article** can be found at:

http://www.sciencemag.org/content/340/6132/630.full.html#related

This article **cites 23 articles**, 11 of which can be accessed free: http://www.sciencemag.org/content/340/6132/630.full.html#ref-list-1

This article has been **cited by** 1 articles hosted by HighWire Press; see: http://www.sciencemag.org/content/340/6132/630.full.html#related-urls

This article appears in the following **subject collections**: Immunology

http://www.sciencemag.org/cgi/collection/immunology

we observed no statistically significant change in the distribution of β values between AGI-5198—and vehicle-treated tumors (Fig. 4B) (supplementary materials).

We next examined the kinetics of histone demethylation after inhibition of the mutant IDH1 enzyme. The histone demethylases JMJD2A and JMJD2C, which remove bi- and trimethyl marks from H3K9, are significantly more sensitive to inhibition by the R-2HG oncometabolite than other 2-OG-dependent oxygenases (8, 9, 14, 25). Restoring their enzymatic activity in IDH1-mutant cancer cells would thus be expected to require near-complete inhibition of R-2HG production. Consistent with this prediction, tumors from the 450 mg/kg AGI-5198 cohort showed a marked decrease in H3K9me3 staining, but there was no decrease in H3K9me3 staining in tumors from the 150 mg/kg AGI-5198 cohort (Fig. 4C) (fig. S11). Of note, AGI-5198 did not decrease H3K9 trimethylation in IDH1-wild-type glioma xenografts (fig. S12A) or in normal astrocytes (fig. S12B), demonstrating that the effect of AGI-5198 on histone methylation was not only dosedependent but also IDH1-mutant selective.

Because the inability to erase repressive H3K9 methylation can be sufficient to impair cellular differentiation of nontransformed cells (16), we examined the TS603 xenograft tumors for changes in the RNA expression of astrocytic (GFAP, AQP4, and ATP1A2) and oligodendrocytic (CNP and NG2) differentiation markers by real-time polymerase chain reaction (RT-PCR). Compared with vehicle-treated tumors, we observed an increase in the expression of astroglial differentiation genes only in tumors treated with 450 mg/kg AGI-5198 (Fig. 4D).

Despite its inability to reverse H3K9 trimethylation and induce gliogenic differentiation markers, the lower dose of AGI-5198 (150 mg/kg) resulted in a similar tumor growth inhibition as the higher dose of AGI-5198 (Fig. 4E) (fig. S13). Induction of the differentiation gene-expression program was thus associated with H3K9me3 demethylation but not required for tumor growth inhibition by AGI-5198, suggesting that mutant IDH regulated proliferation and differentiation in glioma through distinct effector programs with differential sensitivity, kinetic response, or reversibility to the *R*-2HG oncometabolite.

To identify pathways that are associated with the growth-inhibitory effects of AGI-5198, we ran Affymetrix RNA expression arrays. Many of the genes that showed significant changes in expression in both AGI-5198-treated cohorts relate to cardiovascular system development and tissue morphology (table S2) (supplementary materials). Interestingly, vascular abnormalities and disturbed collagen maturation were recently reported as the most prominent phenotype in mice with brain-specific expression of R132H-IDH1 (17).

When viewed on a genome-wide scale, the 150 mg/kg dose of AGI-5198, which was sufficient for maximal growth inhibition, showed only small effects on RNA expression patterns

because 150 mg/kg-treated xenografts clustered with the untreated tumors (fig. S14). Furthermore, an integrated analysis of the DNA methylation and RNA expression data showed no correlation between changes in RNA expression and changes in DNA methylation (fig. S15). Together, these data suggest that mutant IDH1 may promote glioma growth through transcriptional and non-transcriptional mechanisms that are independent of its epigenetic effects.

In summary, we describe a tool compound (AGI-5198) that impairs the growth of R132H-IDH1-mutant, but not IDH1 wild-type, glioma cells. This data demonstrates an important role of mutant IDH1 in tumor maintenance, in addition to its ability to promote transformation in certain cellular contexts (14, 26). Effector pathways of mutant IDH remain incompletely understood and may differ between tumor types, reflecting clinical differences between these disorders. Although much attention has been directed toward TET-family methyl cytosine hydroxylases and Jumonji-C domain histone demethylases, the family of 2-OG-dependent dioxygenases includes more than 50 members with diverse functions in collagen maturation, hypoxic sensing, lipid biosynthesis/metabolism, and regulation of gene expression (27). Our study suggests that a broader investigation of the role of these enzymes in IDH1-mutant glioma may be warranted.

References and Notes

- 1. D. W. Parsons et al., Science 321, 1807 (2008).
- 2. H. Yan et al., N. Engl. J. Med. 360, 765 (2009).
- 3. M. F. Amary et al., J. Pathol. 224, 334 (2011).
- 4. D. R. Borger et al., Oncologist 17, 72 (2012).
- 5. P. Paschka et al., J. Clin. Oncol. 28, 3636 (2010).
- 6. E. R. Mardis et al., N. Engl. J. Med. **361**, 1058 (2009)
- 7. L. Dang et al., Nature 465, 966 (2010).
- 8. M. E. Figueroa et al., Cancer Cell 18, 553 (2010).
- 9. W. Xu *et al.*, *Cancer Cell* **19**, 17 (2011).

- T. Watanabe, S. Nobusawa, P. Kleihues, H. Ohgaki, Am. J. Pathol. 174, 1149 (2009).
- 11. R. G. Verhaak *et al.*; Cancer Genome Atlas Research Network, *Cancer Cell* **17**, 98 (2010).
- 12. H. Noushmehr *et al.*; Cancer Genome Atlas Research Network, *Cancer Cell* **17**, 510 (2010).
- 13. A. Lai et al., J. Clin. Oncol. 29, 4482 (2011).
- 14. P. Koivunen et al., Nature 483, 484 (2012).
- 14. P. Rolvunen et al., Nature **483**, 484 (201). 15. S. Turcan et al., Nature **483**, 479 (2012).
- 16. C. Lu et al., Nature 483, 474 (2012).
- 17. M. Sasaki et al., Genes Dev. 26, 2038 (2012).
- 18. J. Popovici-Muller et al., ACS Medicinal Chem. Lett. 3, 850 (2012).
- 19. D. N. Louis et al., Acta Neuropathol. 114, 97 (2007).
- 20. J. D. Cahoy et al., J. Neurosci. 28, 264 (2008).
- 21. E. S. Lein et al., Nature 445, 168 (2007).
- D. F. Sobieszczuk, A. Poliakov, Q. Xu, D. G. Wilkinson, Genes Dev. 24, 206 (2010).
- 23. R. M. Bachoo et al., Cancer Cell 1, 269 (2002).
- 24. D. K. Ma et al., Nat. Neurosci. 13, 1338 (2010).
- 25. R. Chowdhury et al., EMBO Rep. 12, 463 (2011).
- 26. M. Sasaki et al., Nature 488, 656 (2012).
- M. A. McDonough, C. Loenarz, R. Chowdhury, I. J. Clifton,
 C. J. Schofield, Curr. Opin. Struct. Biol. 20, 659 (2010).

Acknowledgments: We thank W. G. Kaelin Jr., for sharing unpublished results. This work was supported by the National Brain Tumor Society (T.G.G., K.E.Y., and I.K.M.), the National Institutes of Health (1R01NS080944-01 and U54CA143798), the Leon Levy Foundation (I.K.M.), and the James S. McDonnell Foundation (I.K.M.). C.G. was supported through an American Brain Tumor Association Basic Research Fellowship Award and the Lymphoma Research Foundation. T.G.G. is the recipient of a Research Scholar Award from the American Cancer Society. I.K.M. is the recipient of an Advanced Clinical Research Award in Glioma from the American Society of Clinical Oncology. Agios Pharmaceuticals has filed a patent application on AGI-5198. Microarray data are deposited in the Gene Expression Omnibus (GEO accession no. GSE45200).

Supplementary Materials

www.sciencemag.org/cgi/content/full/science.1236062/DC1 Materials and Methods

Supplementary Text Figs. S1 to S16 Tables S1 and S2

Tables S1 and S2 References

4 February 2013; accepted 18 March 2013

Published online 4 April 2013; 10.1126/science.1236062

Disparate Individual Fates Compose Robust CD8⁺ T Cell Immunity

Veit R. Buchholz, Michael Flossdorf, Michael Flossdorf, Lorenz Kretschmer, Bianca Weissbrich, Patricia Gräf, Admar Verschoor, Matthias Schiemann, Homas Höfer, Admar Verschoor, Matthias Schiemann, Michael Flossdorf, Admar Verschoor, Matthias Schiemann, Michael Flossdorf, Matthias Schiemann, Michael Flossdorf, Admar Verschoor, Matthias Schiemann, Michael Flossdorf, Michael Flossdorf, Michael Flossdorf, Admar Verschoor, Matthias Schiemann, Michael Flossdorf, Michael F

A core feature of protective T cell responses to infection is the robust expansion and diversification of naïve antigen-specific T cell populations into short-lived effector and long-lived memory subsets. By means of in vivo fate mapping, we found a striking variability of immune responses derived from individual CD8⁺ T cells and show that robust acute and recall immunity requires the initial recruitment of multiple precursors. Unbiased mathematical modeling identifies the random integration of multiple differentiation and division events as the driving force behind this variability. Within this probabilistic framework, cell fate is specified along a linear developmental path that progresses from slowly proliferating long-lived to rapidly expanding short-lived subsets. These data provide insights into how complex biological systems implement stochastic processes to guarantee robust outcomes.

ollowing Burnet's clonal selection theory (1), a single naïve lymphocyte should be the smallest unit from which an adaptive

immune response can originate, providing both protection to acute infection and lasting memory to reinfection. Indeed, upon infection an individual CD8⁺ T cell can generate a phenotypically and functionally diverse progeny that encompasses both short- and long-lived subsets (2, 3). Thus, individual T cells possess a stunning capacity for diversification (4). However, how this capacity is channeled to generate reproducible immune responses tailored to a specific invading pathogen is unknown. Two mechanisms to achieve this goal can be envisioned: (i) a single—T cell—derived

¹Institute for Medical Microbiology, Immunology and Hygiene, Technische Universität München (TUM), Munich 81675, Germany. ²Division of Theoretical Systems Biology, German Cancer Research Center (DKF2), Heidelberg 69120, Germany. ³BioQuant Center, University of Heidelberg, Heidelberg 69120, Germany. ⁴Clinical Cooperation Groups "Antigen-specific Immunotherapy" and "Immune-Monitoring," Helmholtz Center Munich (Neuherberg), TUM, Munich 81675, Germany. ⁵Focus Group "Clinical Cell Processing and Purification," Institute for Advanced Study, TUM, Munich 81675, Germany. ⁶National Centre for Infection Research (DZIF), Munich 81675, Germany.

response follows a defined expansion and diversification pattern, thus guaranteeing a robust relationship of input and response on the single-cell level; or (ii) this relationship only becomes robust on the level of multiple T cells responding to antigen, as a population integral of variable individual fates. Furthermore, it remains unresolved in which developmental order long- and short-lived subsets arise; different models propose either subset as a predecessor of the other (5, 6) or suggest asymmetric cell division as key to their simultaneous generation (7).

To provide a comprehensive understanding of these issues for CD8⁺ T cells, we have combined an adoptive transfer approach that allows mapping the fate of multiple single-cell-derived progenies in vivo with mathematical modeling. We crossed OT-I T cell receptor (TCR)-transgenic mice, whose CD8⁺ T cells are specific for the SIINFEKL peptide from chicken ovalbumin (OVA) presented on major histocompatibility complex I, to C57BL/6 mice expressing the congenic markers CD45.1 and/or CD90.1 in a homo- or hetero-

zygous fashion. Thereby, we created a matrix of eight TCR-identical OT-I donor lines, distinguishable from one another and from C57BL/6 recipients by their congenic phenotypes (Fig. 1A). Antibody labeling allowed us to discriminate matrix donors from one another and from the CD45.2/ CD45.2-CD90.2/CD90.2 recipient C57BL/6 mice (fig. S1). Successive high-purity single-cell sorting of CD8⁺CD44^{low} cells (fig. S2) displaying homogenous TCR expression levels and naïve phenotype (fig. S3) enabled the assembly of eight individual OT-I matrix cells for subsequent adoptive transfer (fig. S4). To assess the expansion and diversification of single CD8⁺ T cell-derived progenies into effector and memory subsets, we infected recipient mice with recombinant Listeria monocytogenes-expressing OVA (L.m.-OVA). In our hands and as previously shown (8), the differentiation and expansion patterns of low numbers of transferred OT-I T cells closely mirrored those of endogenous SIINFEKL epitope-specific T cells (fig. S5). Simultaneous adoptive transfer

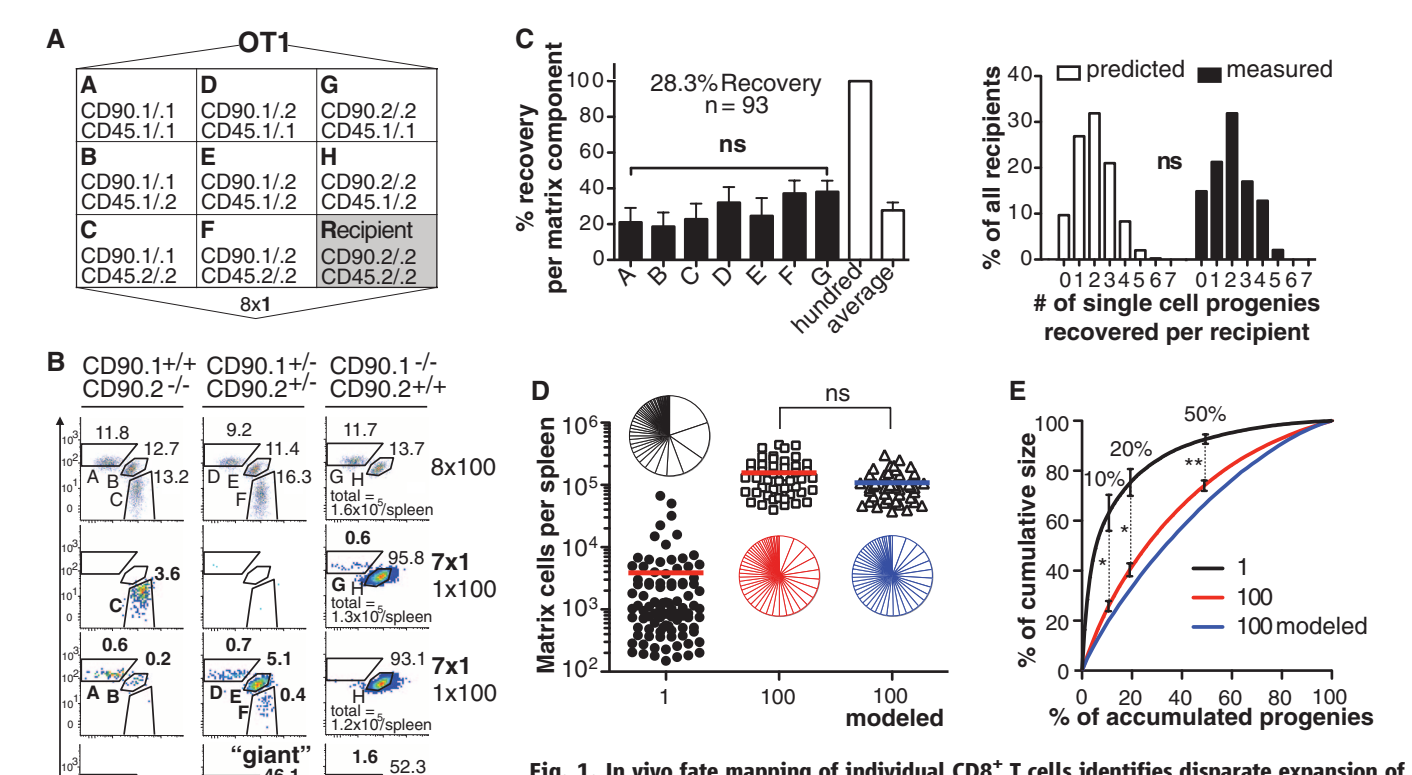


Fig. 1. In vivo fate mapping of individual CD8⁺ T cells identifies disparate expansion of recruited T cells. (A) Scheme depicting genotypes of OT-I congenic matrix donors (A to H) and C57BL/6 recipients (R). (B to E) Progeny recovered from spleen at day 12 after intraperitoneal transfer of CD8⁺CD44^{low} OT-I matrix cells and intravenous infection with 5×10^3 L.m.-OVA. (B) Representative pseudocolor plots of C57BL/6 mice that had received 100 T cells of each matrix phenotype (top row) or a single OT-I cell of each matrix phenotype A to G and 100 of phenotype H

(bottom three rows). Numbers indicate the percentage that a given OT-I matrix population contributes to the combined size of all populations in one recipient. (C) Percent in which progeny could be recovered from single or 100 transferred OT-I cells of matrix phenotype A to G or H, respectively (left). Predicted versus measured distribution of number of single-cell—derived progenies recovered per recipient (right); *n* is the number of single-cell progenies recovered from a total of 47 C57BL/6 recipients; Bars depict mean; error bars indicate SEM. (D) Absolute number of descendants in spleen recovered per transferred single cell (full circles) (n = 93), 100 cells (white squares) (n = 47), or generated by mathematical modeling of 100-cell transfers from single-cell data (white triangles). Each triangle consists of 28 progenies randomly drawn from the single-cell—derived data set. Bars depict mean. Wheel diagrams depict the relative contribution of each progeny to the cumulative size of all. (E) Cumulative size of single-cell—derived (black line), 100-cell—derived (red line), and mathematically modeled progenies (blue line) plotted against the percentage of accumulated progenies. Significant differences of cumulative size are indicated for accumulating the 10, 20, and 50% largest progenies; error bars indicate SEM.

7x1

otal = 5 1.4x10/spleen

CD45.2

1x100

^{*}These authors contributed equally to this work. †Corresponding authors. E-mail: dirk.busch@mikrobio.med. tum.de (D.H.B.); t.hoefer@dkfz-heidelberg.de (T.H.)

of 100 OT-I T cells of each matrix phenotype ("8×100" transfer) led to comparable expansion and subset diversification of all eight matrix populations (Fig. 1B, top row, and fig. S6).

To compare the progenies of individual cells and cell populations, every C57BL/6 recipient received seven single-matrix OT-I cells (matrix components A to G) and one congenic population consisting of 100 matrix OT-I cells (matrix component H) in a combined "7×1 plus 1×100" transfer (Fig. 1B). Independent of matrix phenotype, descendants were recovered from ~28% of transferred single cells (Fig. 1C). This indicates that a transferred 100-cell matrix population contributes on average 28 detectable single-cellderived progenies to the overall response. Indeed, the means of single- and 100-cell-derived progeny sizes scaled according to this prediction (Fig. 1D). However, size distribution of single-cellderived progenies was remarkably broad, ranging over three orders of magnitude (Fig. 1D). By day 12 after infection, most single cells had generated numbers of descendants well below the mean of ~4000 cells per spleen ("dwarfs"), whereas very few expanded massively, generating up to 70,000 descendants ("giants") (Fig. 1, B, bottom row, and D). The number of descendants recovered from the spleen tightly correlated to a progeny's overall expansion in spleen, lung, and lymph nodes (fig. S7). Highly disparate single-cell-derived expansion occurred within individual recipients (Fig. 1B, bottom) and could neither be accounted for by inter-individual infection variability nor variable expression of additional TCRs on transferred OT-I T cells (figs. S8 and S9). We could recreate in silico the much narrower distribution of 100-cellderived populations through repetitively drawing 28 random samples from our single-cell-derived data set (Fig. 1, D and E). The skewed size distribution of single-cell progenies leads to 5% of naïve precursors generating over 50% of all descendants (Fig. 1E). Similarly skewed expansion patterns were observed before the contraction phase, at day 8 after infection (fig. S10), making it unlikely that cell death substantially shapes disparate single-cell-derived progeny sizes. Single-cell-derived responses remained equally skewed when individual precursors were transferred without a 100-cell control population (fig. S11), excluding any unphysiological competitive pressure as the cause of skewness. A different immunization using systemic infection with Vaccinia virus-expressing OVA (Vaccinia-OVA) yielded congruent results (fig. S12). Thus, within a monoclonal population of T cells the bulk of infection-driven expansion is based on the proliferative activity of a small fraction of recruited

To probe the physiological consequences of heterogeneous single-cell-derived expansion, we analyzed surface markers associated with memory development. Strikingly, most single-cell-derived progenies expressed significantly higher levels of memory markers CD62L (9) and CD27 (10) than expected from the expression patterns

of 100-cell–derived populations (Fig. 2, A to C, and figs. S13 and S14). However, the rare single-cell progenies that had expanded to giants were strongly biased for CD27⁻CD62L⁻ effector phenotype (Fig. 2D, top left). This inverse relation between proliferation and memory phenotype (Fig. 2, D to F, and figs. S13 and S14) accounts for the different distribution of memory markers in single-cell progenies and 100-cell-derived populations, as shown by composing 100-cell transfer data from single-cell progenies in silico (Fig. 2, B and C).

Next, we studied the production of cytokines. Autochthonous interleukin-2 (IL-2) production during primary infection signifies memory or memory precursor cells (9, 11, 12). Coproduction of interferon-γ (IFN-γ) is characteristic of multifunctional cells, the presence of which is thought to predict vaccination success (13). Similar to the expression pattern of surface memory markers, most single-cell–derived progenies showed a higher percentage of IL-2 and IFN-γ producers than expected from population analysis (Fig. 3, A to C). Whereas expression of IL-2 was essen-

tially absent and IFN-y production low in giant progenies with a dominant effector phenotype, the opposite was true for the abundant dwarfs (Fig. 3, D to F). These also expressed less T-box transcription factor expressed in T cells (T-bet) and showed a trend toward higher eomesodermin (Eomes) expression than that of their giant counterparts (Fig. 3G). The association of Eomes with memory and T-bet with terminal effector fate (14–16) was further confirmed by their opposing correlation patterns in relation to expression of CD62L, CD27, and short-lived effector cell marker Killer-cell-lectin-like-receptor-G1 (KLRG1) (Fig. 3H) (17). Thus, heterogeneous single-T cellderived expansion was reproducibly accompanied by a relative reduction of memory precursor characteristics—on the level of phenotype, function, and transcription factor expression.

To alter stimulus strength, we delayed transfer of single T cells to day 3 after infection. As expected, this reduced mean response size (18). However, size variability between single-cell progenies remained virtually unaffected (fig. S15).

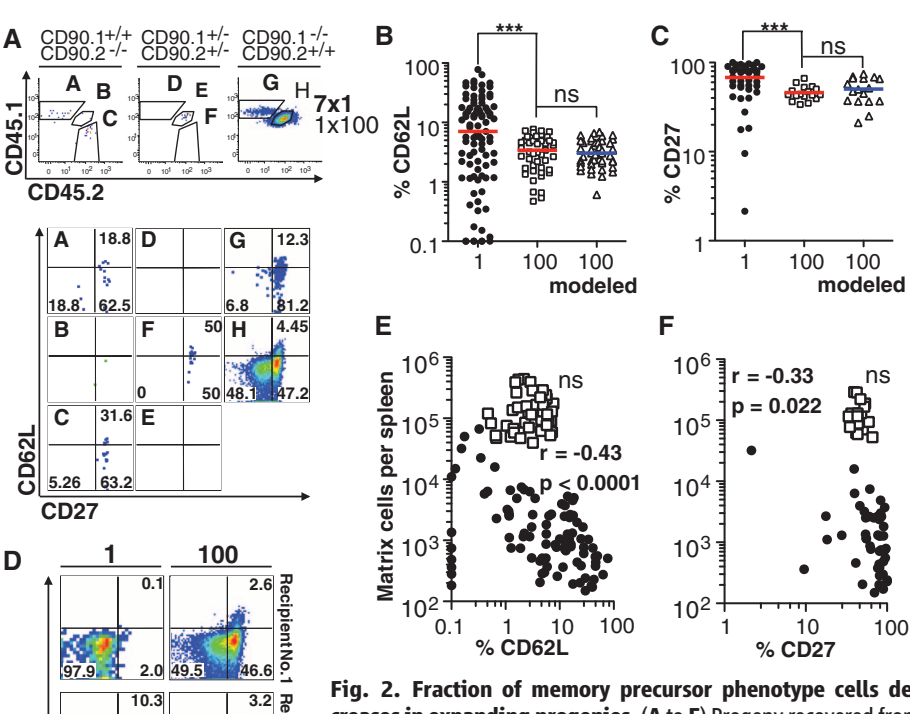


Fig. 2. Fraction of memory precursor phenotype cells decreases in expanding progenies. (**A** to **F**) Progeny recovered from the spleens of 47 C57BL/6 recipient mice at day 12 after intraperitoneal transfer of CD8 $^+$ CD44 low OT-I matrix cells and intravenous infection with 5×10^3 *L.m.*-OVA. C57BL/6 mice received a single OT-I cell of each matrix phenotype A to G and 100 cells of phenotype H. (A) Representative pseudo-color plots showing size as well as CD27 and CD62L phenotype of expanded progenies in one recipient. (B) Scatter plots depict percentage of CD62L-expressing cells of single-cell—derived (full circles) (n = 93), 100-cell—derived (white squares) (n = 47), or 100-cell—derived progenies mathemat-

ically modeled from the single-cell—derived data set (white triangles). Bars indicate median. (C) As in (B), but for percentage of CD27-expressing cells. (D) Representative pseudo-color plots showing CD27 and CD62L expression of large to small single-cell—derived progenies together with phenotype of 100-cell—derived progenies in the same recipients. (E) Scatter plots depict correlation of size and percentage of CD62L-expressing cells of single-cell—derived (full circles) and 100-cell—derived progenies (white squares). (F) As in (E), but for percentage of CD27-expressing cells.

45.5

CD27

Thus, global alteration of immune response parameters proved unfit to reach mechanistic insight into how variability develops on the single-cell level. To provide more insight, we asked whether single-cell progenies at the peak of the immune response contain a "footprint" of their individual differentiation and proliferation histories. For unbiased computational analysis of this question, we constructed all possible diversification pathways of a single naïve cell into three derived subsets: central memory precursor (TCMp; CD27⁺CD62L⁺), effector memory precursor (TEMp; CD27⁺CD62L⁻), and effector cells (TEF; CD27 CD62L). Allowing for both unidirectional and reversible differentiation steps and subset-specific proliferation rates, we obtained 304 distinct pathways of T cell diversification from the general scheme (Fig. 4A) and translated these into stochastic dynamic models (fig. S16) (19-21). Only two models provided a good fit to the experimental data, with all parameter values being identifiable within narrow bounds (Fig. 4B and fig. S17). All remaining 302 models fit the data poorly (Fig. 4C and fig. S18). The two fitting models predict a linear framework of differentiation, following the pathway naïve→TCMp→TEMp→TEF

[in Fig. 4B, model 1, ~10% of cells develop directly from naïve to TEMp, which could be due to a fraction of naïve cells dividing asymmetrically (fig. S19); model 2 fits the data nearly as well without this transition]. The proliferation rates increase along this pathway, with TCMp cells proliferating substantially slower than TEMp and TEF cells (figs. S17 and S19). The linear diversification model correctly reproduces the inverse correlation between memory marker (CD62L and CD27) abundance and size of single-cell progenies at day 8 after infection (Fig. 4D and fig. S20). To further test the model, we simulated and subsequently measured these sizes and correlations at day 6 after infection (Fig. 4D and fig. S21) as well as the proliferation rates at days 3 and 4 after infection (fig. S22), finding agreement between model and experimental data. Relying only on single-cell progeny data from day 8 after infection, the model correctly predicted the phenotypic composition of an expanding T cell population over days 1 to 8 after infection (Fig. 4E and fig. S22). Thus, our data imply a linear framework of CD8⁺ T cell differentiation, with slowly proliferating memory precursors giving rise to rapidly expanding effector cells.

Our model identifies the initial events in each single-cell progeny's developmental history as the drivers of variability. As long as the number of daughter cells is very low (up to ~10 descendants), the stochastic timing of proliferation and differentiation events (mediated through intrinsic and/or extrinsic cues) will cause individual progenies to differ strongly from one another. These differences are stably propagated when larger cell numbers are reached (Fig. 4F). In particular, the early transition of single-cell-derived descendants into higher proliferative states can give rise to giants dominated by rapidly expanding TEMp and TEF cells (fig. S23). Overall, our data imply that robustness of CD8⁺ T cell immune responses requires participation of ~50 naïve progenitors (fig. S24).

Single-cell progeny size correlated strongly with the size of TEMp and TEF compartments and only weakly with the absolute number of TCMp cells (Fig. 4G), despite the existence of a strong inverse correlation between the relative fraction of TCMp cells and progeny size (Fig. 4D, left). This implies that a progeny's primary size is a poor predictor of its expansion potential upon secondary challenge. To examine this

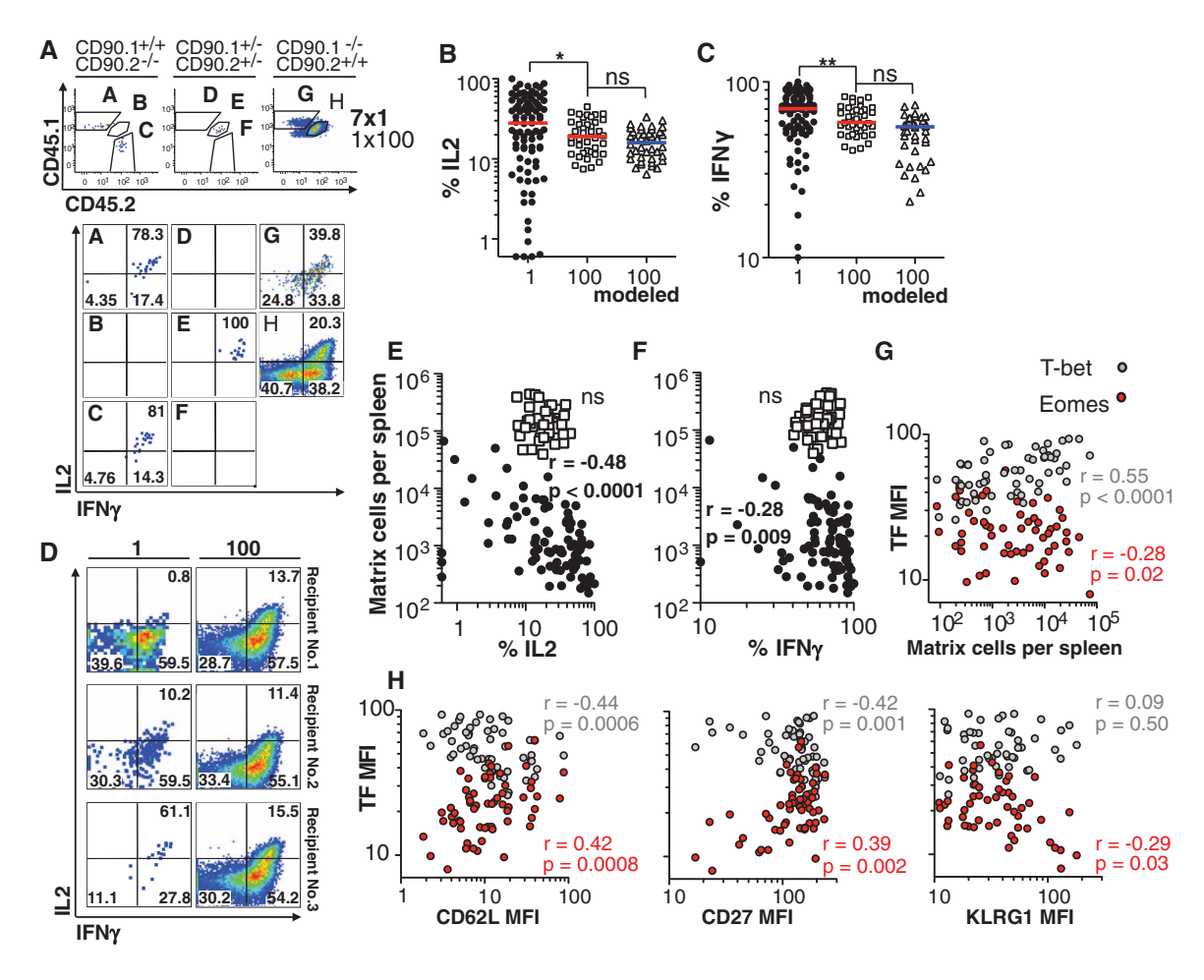


Fig. 3. Fraction of cells with memory precursor function and respective transcription factor profile decreases in expanding progenies. (A to F) As in Fig. 2, A to F, but for percentage of IL-2— and IFNγ-expressing

cells. (**G** and **H**) Scatter plots depict mean fluorescence intensity (MFI) of Eomes (red dots) and T-bet (gray dots) correlated to (G) size or (H) MFI of CD62L, CD27, and KLRG1 of single-cell—derived progenies.

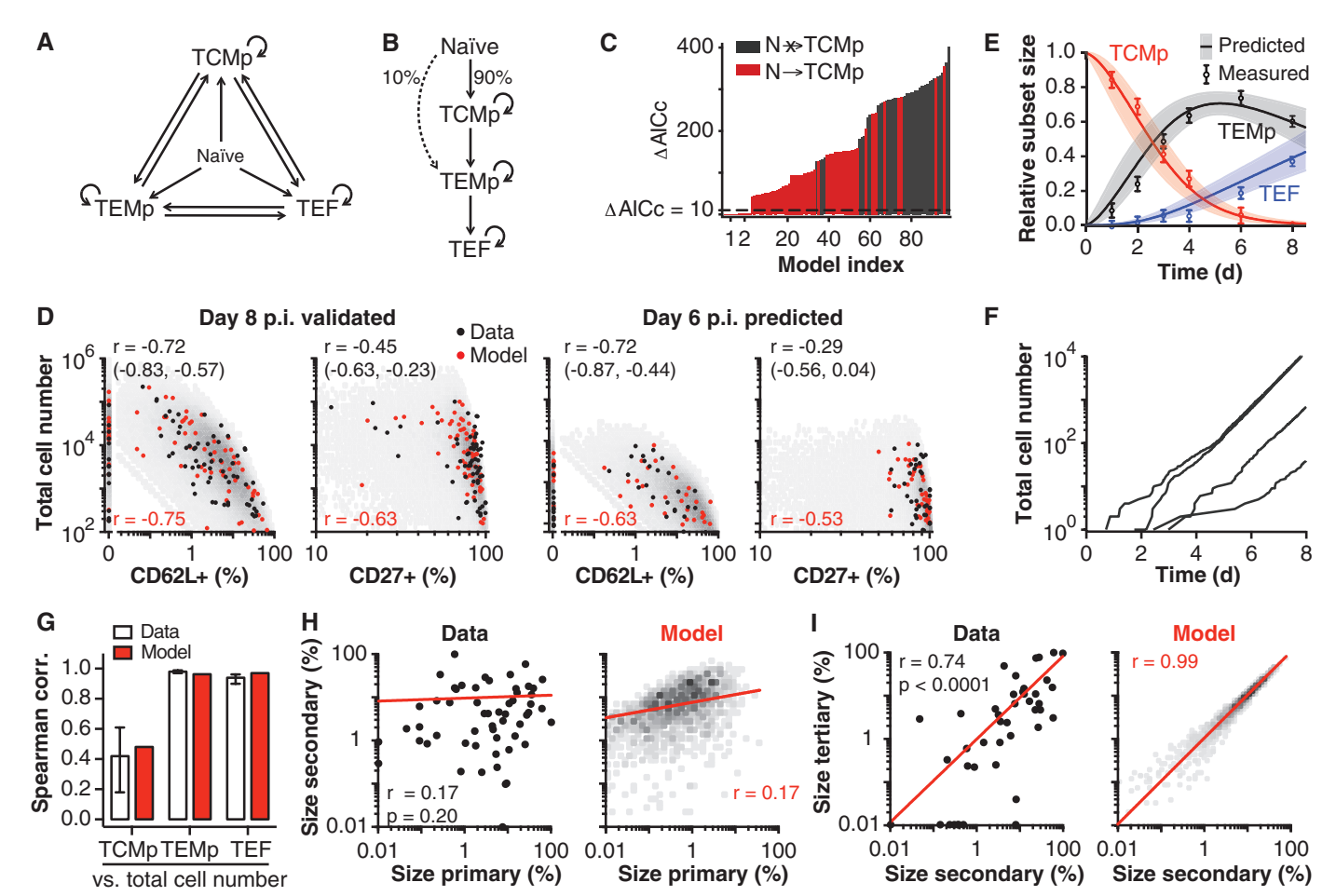


Fig. 4. Stochastic progression along a linear differentiation pathway underlies CD8⁺ T cell diversification. (A) Model scheme allowing for all possible diversification pathways from naïve to TCMp, TEMp, and TEF subsets, with subset-specific differentiation (straight arrows) and proliferation (curved arrows) rates. (B) Unique model structure that accounts for the experimental data. (C) Model ranking with corrected Akaike information criterion; models having △AICc > 10 are essentially unsupported by the data. Red bars indicate models including a naïve→TCMp differentiation step; gray bars indicate other models. (D) As in Fig. 2, E and F, but for days 8 and 6 after infection; measured single-cell—derived progenies (black dots), equal number of stochastic simulations (red dots), and probability density (gray scale) of naïve→TCMp→TEMp→TEF model. p.i., post-infection. (E) Relative subset sizes at days 1 to 8 after infection predicted with the model ex-

clusively from day 8 single-cell progeny data (filled regions indicate 95% prediction bands) and measured (circles) after transfer of 10,000 (days 1 to 4) or 100 OTI cells (days 6 and 8). Error bars indicate SEM and are based on pooled variance for days 1 to 6. (**F**) Four simulations of single-cell progeny expansion. (**G**) Correlation of absolute TCMp, TEMp, and TEF number versus total cell number; error bars, 95% confidence interval. (**H** and **I**) Data (left) and model prediction (right) for relation of (H) primary versus secondary and (I) secondary versus tertiary response size (largest progeny = 100%, others scaled accordingly); log-log regression (red line); experiment performed as in Fig. 2, but progenies recovered from peripheral blood at day 8 after primary (day 8 after infection), day 6 after secondary (day 42 after infection), and day 6 after tertiary infection (day 235 after infection) with $5 \times 10^3 \ L.m.$ -OVA, $1 \times 10^5 \ L.m.$ -OVA, and $1 \times 10^8 \ MVA$ -OVA, respectively.

hypothesis, we monitored the peak size of singlecell-derived progenies during primary and secondary immune responses (fig. S25). Indeed, peak size during secondary challenge was nearly uncorrelated to primary progeny size, allowing some "dwarfs" to expand up to 200-fold in relation to their primary size (Fig. 4H). However, when animals were subjected to heterologous tertiary challenge with Modified Vaccinia Ankaraexpressing OVA (MVA-OVA), we observed a strong correlation to secondary response size (Fig. 4I). Both data sets are in accord with the naïve→TCMp→TEMp→TEF model when recall expansion is assumed to originate mainly from TCMp populations (Fig. 4, H and I). Together with similar findings gathered by means of genetically labeling individual T cells (22), these

observations argue that memory content is not predicted by a single-cell progeny's primary, effectordominated expansion, yet there is a robust and predictable expansion pattern of recall responses originating from populations of multiple memory cells.

Collectively, our data suggest that the early developmental histories of single-cell-derived progenies shape their disparate fates, which compose robust immunity only together, as distinct variations on a shared developmental theme. Our findings are reminiscent of stochastic precursor progeny dynamics and proliferative hierarchies, recently described as essential for stem cell-based maintenance of tissue homeostasis (23, 24). By shedding light on how the descendants of individual T cells compose complex immune re-

sponses, we provide a framework for the strategic design of future vaccination and adoptive immunotherapy approaches.

References and Notes

- 1. F. M. Burnet, *The Clonal Selection Theory of Acquired Immunity* (Cambridge Univ. Press, Cambridge, UK, 1959).
- 2. C. Stemberger et al., Immunity 27, 985 (2007).
- 3. C. Gerlach et al., J. Exp. Med. 207, 1235 (2010).
- 4. S. L. Reiner, F. Sallusto, A. Lanzavecchia, *Science* **317**, 622 (2007).
- 5. E. J. Wherry et al., Nat. Immunol. 4, 225 (2003).
- 6. A. V. Gett, F. Sallusto, A. Lanzavecchia, J. Geginat, Nat. Immunol. 4, 355 (2003).
- 7. J. T. Chang et al., Science 315, 1687 (2007).
- 8. V. P. Badovinac, J. S. Haring, J. T. Harty, *Immunity* **26**, 827 (2007).
- F. Sallusto, D. Lenig, R. Förster, M. Lipp, A. Lanzavecchia, Nature 401, 708 (1999).
- 10. H. Hikono et al., J. Exp. Med. 204, 1625 (2007).

- M. A. Williams, A. J. Tyznik, M. J. Bevan, *Nature* 441, 890 (2006).
- 12. S. Feau, R. Arens, S. Togher, S. P. Schoenberger, *Nat. Immunol.* **12**, 908 (2011).
- R. A. Seder, P. A. Darrah, M. Roederer, *Nat. Rev. Immunol.* 8, 247 (2008).
- 14. A. Banerjee et al., J. Immunol. 185, 4988 (2010).
- 15. X. Zhou et al., Immunity 33, 229 (2010).
- 16. N. S. Joshi et al., Immunity 27, 281 (2007).
- 17. D. Voehringer et al., J. Immunol. 167, 4838 (2001).
- W. N. D'Souza, S. M. Hedrick, J. Immunol. 177, 777 (2006).
- J. E. Till, E. A. McCulloch, L. Siminovitch, *Proc. Natl. Acad. Sci. U.S.A.* 51, 29 (1964).
- 20. K. R. Duffy et al., Science 335, 338 (2012).

- Materials and methods are available as supplementary materials on Science Online.
- 22. C. Gerlach et al., Science 340, 635 (2013).
- 23. B. D. Simons, H. Clevers, Cell 145, 851 (2011).
- 24. G. Mascré et al., Nature 489, 257 (2012).

Acknowledgments: The authors thank L. Henkel for cell sorting; A. Muschaweckh and I. Drexler for providing Vaccinia-OVA and MVA-OVA; and K. Kerksiek, H. Wagner, C. Stemberger, F. Anderl, S. Dreher, and T. G. Grünewald for helpful discussion and/or critically reading the manuscript. The authors declare no conflict of interest. The data presented in this manuscript are tabulated in the main paper and in the supplementary materials. This work was supported by the SFB TR 36 (TP-B10/13, TP-Z1), the SFB 1054 (TP-B09), the

SFB 914 (TP-B04), the Initiative and Networking Fund of the Helmholtz Association within the Helmholtz Alliance on Immunotherapy of Cancer, EU-FP7 SYBILLA (201106), BMBF ForSysPartner (0315267E), and by the National Science Foundation under grant NSF PHY11-25915.

Supplementary Materials

www.sciencemag.org/cgi/content/full/science.1235454/DC1 Materials and Methods Figs. S1 to S27 References (25–28)

22 January 2013; accepted 7 March 2013 Published online 14 March 2013; 10.1126/science.1235454

Heterogeneous Differentiation Patterns of Individual CD8⁺ T Cells

Carmen Gerlach, 1*† Jan C. Rohr, 1,2* Leïla Perié, 1,3 Nienke van Rooij, 1 Jeroen W. J. van Heijst, 1‡ Arno Velds, 4 Jos Urbanus, 1 Shalin H. Naik, 1§ Heinz Jacobs, 5 Joost B. Beltman, 1,3 Rob J. de Boer, 3 Ton N. M. Schumacher 1

Upon infection, antigen-specific CD8⁺ T lymphocyte responses display a highly reproducible pattern of expansion and contraction that is thought to reflect a uniform behavior of individual cells. We tracked the progeny of individual mouse CD8⁺ T cells by in vivo lineage tracing and demonstrated that, even for T cells bearing identical T cell receptors, both clonal expansion and differentiation patterns are heterogeneous. As a consequence, individual naïve T lymphocytes contributed differentially to short- and long-term protection, as revealed by participation of their progeny during primary versus recall infections. The discordance in fate of individual naïve T cells argues against asymmetric division as a singular driver of CD8⁺ T cell heterogeneity and demonstrates that reproducibility of CD8⁺ T cell responses is achieved through population averaging.

he murine naïve T cell repertoire contains about 100 to 1000 CD8 $^+$ T cells specific for a given antigen (1, 2), which upon antigen-recognition proliferate to produce up to 10^7 progeny (2-4). After pathogen clearance, the numbers of antigen-specific T cells decline by 90 to 95%, leaving behind a population of memory T cells (5). This characteristic T cell response kinetic is accompanied by differentiation into functionally distinct subsets (6, 7).

Although the patterns of T cell differentiation and response kinetics are highly reproducible for a given infection, it is unclear how this reproducibility is controlled. Single-cell tracing studies have unambiguously shown that individual naïve

individual naïve T cells to the effector and memory pools has not been determined. Reproducibility of T cell responses could be controlled at the single-cell level, with each naïve T cell producing the same types and amount of progeny, and asymmetric division of T cells (10) would provide a mechanism to ensure such equal representation. Alternatively, individual T cell families (i.e., one naïve T cell and its progeny) may show distinct sizes or phenotypes, with reproducibility manifesting itself only at the population level. Both scenarios predict very different mechanisms behind protection to renewed infection. In the former, a defined fraction of each family provides long-term memory; in the latter, some T cell families could primarily convey short-term protection, whereas others could mostly yield memory cells.

T cells are able to yield both effector and memory

cells (8, 9). However, the relative contribution of

We aimed to distinguish between these two potential mechanisms for T cell reactivity during primary and renewed infections by in vivo lineage tracing of individual naïve CD8⁺ T cells. Combination of a previously established DNA barcode-based lineage tracing technology (9, 11–13) with second-generation sequencing allowed quantification of individual T cell families with substantial accuracy [quantification and correction procedures are described in fig. S1 and (14)]. To track individual T cells in a system in which dif-

ferences in T cell receptor (TCR) affinity do not influence cell fate, we generated naïve TCR-transgenic OT-I T cells [which recognize the SIINFEKL (E, Glu; F, Phe; I, Ile; K, Lys; L, Leu; N, Asn; and S, Ser) peptide presented on H-2K^b] that each carry a unique DNA barcode (9). Mice transferred with physiological numbers of these cells were then infected with *Listeria monocytogenes* expressing SIINFEKL (LM-OVA), and barcode sequencing was used to quantify the progeny of individual naïve T cells.

Analysis of the contribution of individual T cells at the peak of the immune response revealed the number of progeny produced by individual T cells to be highly variable (Fig. 1A, controls in fig. S2) and, on average, the "dominant" naïve T cell produced 400-fold more offspring than the median naïve T cell within the same animal (Fig. 1B). As a consequence, about 60% of the total OT-I T cell pool was derived from only 5% of naïve OT-I cells (Fig. 1C). Although ~50% of OT-I families consisted of fewer than 200 daughter cells, these minifamilies had formed as a consequence of TCR triggering rather than bystander or homeostatic proliferation (fig. S3A). The numerical dominance of a small number of T cell families was unrelated to rearrangement of the endogenous TCR loci, because LM-OVA-induced responses of OT-I Rag2^{-/-} T cells were also biased toward few families (fig. S3, B to D). Furthermore, family-size disparity was independent of the number of responding OT-I families (range evaluated:17 to 874 families per animal, fig. S3E), arguing against competition between the transferred cells as a confounding factor.

To evaluate whether these results were influenced by the retroviral integration sites of barcodes, we developed a transgenic mouse strain (BCM) that allows DNA barcode generation in vivo at a defined genomic locus (fig. S4A). After LM-OVA infection, OT-I T cells harboring such endogenously generated barcodes also displayed a marked variability in clonal output (fig. S4, B and C). Thus, T cell fate is also disparate when cells are tagged at a specific genomic site.

Strong disparity in the number of progeny of different naïve T cells constitutes a robust feature of T cell responses, observed upon infection with different doses of LM-OVA (Fig. 1D), in high- and low-affinity TCR-antigen interactions (Fig. 1E) and upon pulmonary influenza infection

¹Division of Immunology, Netherlands Cancer Institute, Amsterdam, Netherlands. ²Centre of Chronic Immunodeficiency (CCI), University Medical Centre Freiburg and University of Freiburg, Freiburg, Germany. ³Theoretical Biology and Bioinformatics, Utrecht University, Utrecht, Netherlands. ⁴Central Genomics Facility, Netherlands Cancer Institute, Amsterdam, Netherlands. ⁵Division of Biological Stress Responses, Netherlands Cancer Institute, Amsterdam, Netherlands.

*These authors contributed equally to this work. †Present address: Department of Microbiology and Immunobiology, Harvard Medical School, Boston, MA 02115, USA. ‡Present address: Immunology Program, Sloan-Kettering Institute, Memorial Sloan-Kettering Cancer Center, New York, NY 10065, USA.

§Present address: Division of Immunology, The Walter and Eliza Hall Institute of Medical Research, 1G Royal Parade, Parkville Victoria 3052, Australia.

||Corresponding author. E-mail: t.schumacher@nki.nl